Volume 1
Number 2
March 2023
Pages 97–172

EES Catalysis

rsc.li/EESCatalysis

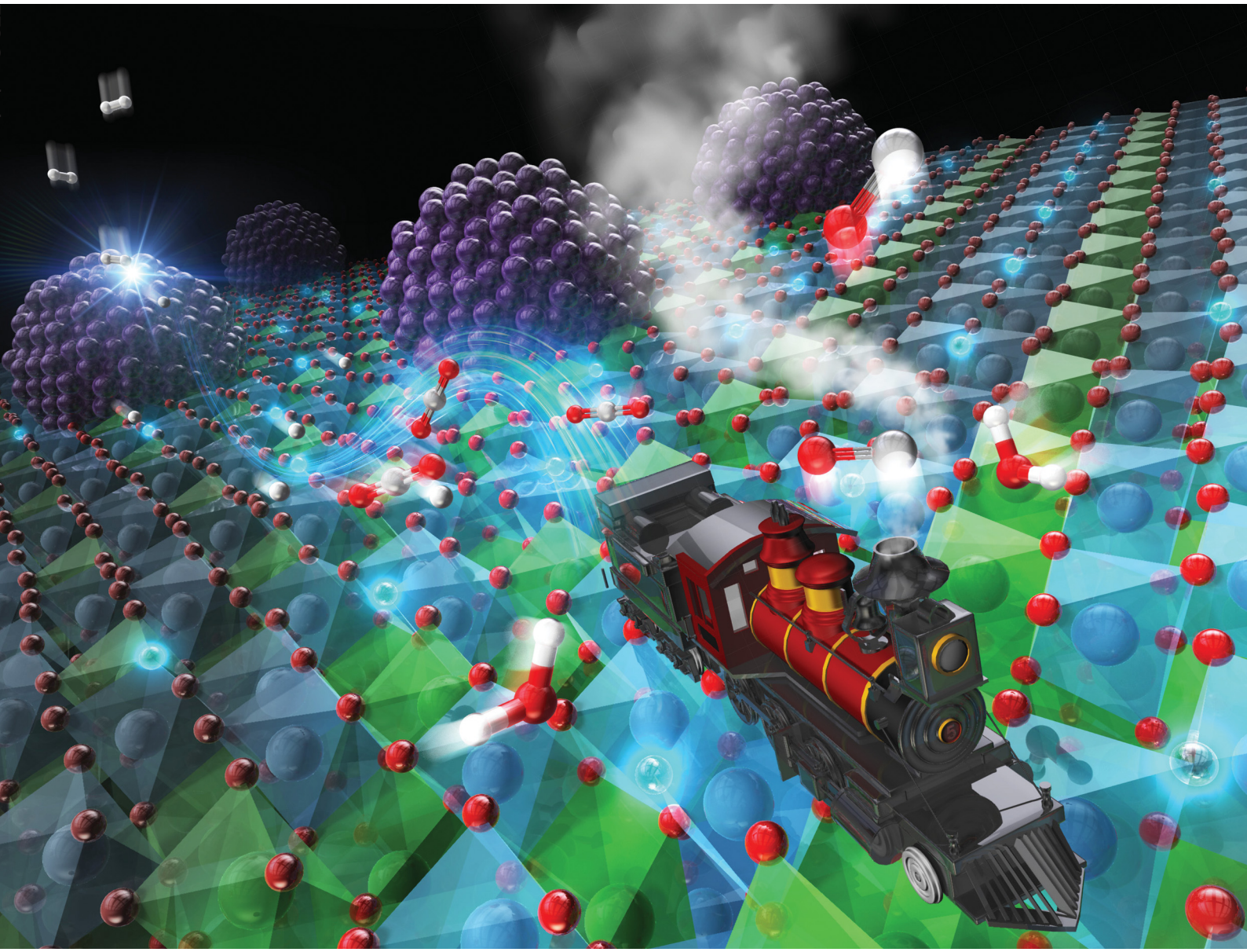

ISSN 2753-801X

ROYAL SOCIETY OF CHEMISTRY

PAPER

Yasushi Sekine *et al.*

Non-conventional low-temperature reverse water–gas shift reaction over highly dispersed Ru catalysts in an electric field

EES Catalysis

PAPER

View Article Online
View Journal | View Issue

Cite this: *EES Catal.*, 2023, 1, 125

Non-conventional low-temperature reverse water–gas shift reaction over highly dispersed Ru catalysts in an electric field†

Ryota Yamano,[a] Shuhei Ogo,[b] Naoya Nakano,[a] Takuma Higo[a] and Yasushi Sekine*[a]

Received 10th August 2022,
Accepted 11th November 2022

DOI: 10.1039/d2ey00004k

rsc.li/eescatalysis

The reverse water–gas shift (RWGS) reaction, a promising carbon-recycling reaction, was investigated by applying an electric field to promote the reaction at a temperature of 473 K or lower. The highly dispersed $Ru/ZrTiO_4$ catalysts with an approximately 2 nm particle size of Ru showed high RWGS activity with a DC electric field below 473 K, whereas CO_2 methanation proceeded predominantly over catalysts with larger Ru particles. The RWGS reaction in the electric field maintained high CO selectivity, suppressing CO hydrogenation into CH_4 on the Ru surface by virtue of promoted hydrogen migration (surface protonics). The reaction mechanisms of the non-conventional low-temperature reverse water gas shift reaction were investigated and revealed using various characterization methods including *in situ* diffuse reflectance infrared Fourier transform spectroscopy (DRIFTS) measurements. With the DC electric field, the reaction proceeds *via* a redox reaction where the generated oxygen vacancies are involved in CO_2 activation at low temperatures. As a result, the electric field promotes both hydrogen migration and redox reactions using lattice oxygen/vacancies, resulting in high RWGS activity and selectivity even at low temperatures.

Broader context

For establishing carbon recycling processes, the reverse water gas shift reaction is a very important reaction. Due to the large endothermic reaction, the reaction does not proceed very well at low temperatures with conventional catalyst technology. In addition, at low temperatures, the side reaction, methanation, which is an exothermic reaction, occurs concurrently and dominates. We have discovered and established a new catalytic process that can selectively and rapidly proceed only with the reverse water gas shift on a fine Ru catalyst at temperatures as low as 473 K by means of a non-conventional catalytic process in which an electric field is applied. The reaction mechanisms of the reverse water gas shift on the non-conventional catalytic process were investigated and revealed by *in situ* diffuse reflectance infrared Fourier transform spectroscopy (DRIFTS) measurements and other characterizations. These revealed that CO hydrogenation into CH_4 on the Ru surface was suppressed by virtue of promoted hydrogen migration (surface protonics). Our findings contribute to the establishment of efficient and selective CO_2 conversion catalysis which can work at a low temperature of 473 K.

Introduction

Recently, many countries have set a goal of reducing CO_2 emissions, virtually to zero, during a half-century. Various efforts are being made to develop the necessary associated technologies.[1] Catalytic conversion of CO_2 with green hydrogen has drawn much attention from the perspective of CO_2 capture and utilization (CCU).[2,3] Numerous studies have revealed that CO_2 can be converted into basic chemical building blocks such as methane (CH_4),[4] carbon monoxide (CO),[5] methanol (CH_3OH),[6] and more complex chemical compounds.[7–9]

Particularly, carbon monoxide, produced in the reverse water–gas shift (RWGS) reaction (eqn (1)), plays a central role in C1 chemistry, by which CO can be converted further to value-added chemicals such as hydrocarbons for liquid fuels *via* Fischer–Tropsch (FT) synthesis and oxygenated compounds through well-established industrial processes.[5] However, the RWGS reaction is endothermic $\left(\Delta H^{\circ}_{298} = 41.2\ \text{kJ mol}^{-1}\right)$. Therefore, the activity is constrained heavily by thermodynamic equilibria. As a matter of fact, achieving 50% conversion requires extremely high temperatures of over 1000 K.

$$CO_2 + H_2 \rightarrow CO + H_2O, \quad \Delta H^{\circ}_{298} = 41.2\ \text{kJ mol}^{-1} \qquad (1)$$

[a] *Department of Applied Chemistry, Waseda University, 3-4-1, Okubo, Shinjuku, Tokyo, 169-8555, Japan. E-mail: ysekine@waseda.jp*
[b] *Department of Marine Resources Science, Faculty of Agriculture and Marine Science, Kochi University, Nankoku, 783-8502, Japan*

† Electronic supplementary information (ESI) available. See DOI: https://doi.org/10.1039/d2ey00004k

In recent years, unconventional catalytic reaction processes such as electrocatalysis,[10] photocatalysis,[11] chemical looping,[12] and plasma application[13] have been attempted for CO_2 conversion under milder conditions. We succeeded in the enhancement of some catalytic reactions in lower-temperature regions by application of an electric field to catalysts. In the system, a weak direct current is imposed on the catalyst bed. The activated surface proton migration induces a new reaction pathway that differs from that of the conventional thermal catalytic reaction: the Langmuir–Hinshelwood mechanism. For example, during CH_4 steam reforming,[14] ammonia synthesis[15] and the dehydrogenation of methylcyclohexane,[16] proton hopping *via* surface hydroxyl species derived from H_2O or H_2 is promoted in an electric field. The dissociation of solid bonds such as C–H and N–N bonds is assisted by H^+ collision at the metal–support interface.

As earlier work, we have applied electric fields for several reactions including carbon dioxide activation (RWGS,[17] dry reforming of methane,[18,19] oxidative coupling of methane using carbon dioxide,[20] and CO_2 methanation[21]). Nevertheless, how CO_2 is activated in catalytic reactions with an electric field remains unclear. Moreover, in our latest study of CO_2 methanation in an electric field, kinetic analysis and spectroscopic measurements revealed that this reaction pathway included CO formation *via* RWGS, which is the rate-determining step. In addition, this reaction exhibited structural sensitivity in which Ru catalysts with a lower loading weight were favorable for the formation of CO, regarded as the by-product in this system. These findings suggest that the smaller Ru-particle-supported (highly dispersed) catalysts are rather suitable for the RWGS reaction. Tuning selectivity for CO_2 hydrogenation has been examined in earlier studies, particularly addressing the necessity of sufficient sites for CO hydrogenation on the active metal surface and modification of the morphology or the electronic state of the metal associated with the stability of intermediates of the reaction.[22–26]

In this work, we aimed to use an electric field for the selective RWGS reaction to achieve high activity at lower temperatures and to shed light on the reaction mechanism of catalytic CO_2 activation in the electric field. The catalysts appropriate for this reaction were prepared *via* the synthesis of colloidal Ru nanoparticles using the chemical reduction method and deposition on the supports because the conventional impregnation method produces large particle size distributions unless the Ru loading weight is decreased drastically. After confirming the structure of the synthesized Ru nanoparticles through characterizations, these catalysts were shown to exhibit high RWGS selectivity (>90%) in the low-temperature region of less than 423 K with the electric field. Furthermore, we evaluated the role of the electric field in the catalytic RWGS reaction through a comparative study of the activity behavior with conventional heated catalysis.

Experimental

Catalyst preparation

The catalyst supports were prepared using a complex polymerization method that includes the use of citric acid and ethylene glycol. Following the addition of citric acid and ethylene glycol to purified water, appropriate metal precursors were mixed with this solution. All reagents were obtained from Kanto Chemical Co. Inc. The precursors are presented in Table S1 (ESI†). The solution was stirred at 343 K for 18 h and then heated with a hot stirrer at 673 K to evaporate the water. The obtained resin was calcined at 673 K for 2 h with pre-calcination and then at 1073 K for 10 h to remove the residual carbons completely.

In an attempt to prepare highly dispersed Ru catalysts, Ru nanoparticles were synthesized *via* colloidal synthesis using the liquid-phase reduction by ethylene glycol as described in several reports,[27–29] but with slight modifications. First, tris(acetylacetonato)ruthenium(III) ($Ru(acac)_3$, Tanaka Holdings Co., Ltd) was dissolved in 100 mL of ethylene glycol, which served as a reducing agent and solvent. After the addition of 10 mL of 1 M NaOH (Kanto Chemical Co. Inc.) aqueous solution to promote reduction, it was heated to 473 K and stirred for 2 h. The obtained colloidal solution of Ru nanoparticles was separated by centrifugation, washed thoroughly with ethanol, and dried at room temperature overnight. These colloidal nanoparticles were then re-dispersed in purified water. Subsequently, after this colloidal solution was mixed with supports and stirred for 5 h at room temperature, the suspension was filtered and dried at 393 K overnight. Finally, the resulting powder was treated under a reducing atmosphere (50% H_2 flow) at 723 K for 2 h.

Catalyst preparation using a typical impregnation method was conducted to compare the activity among catalysts with different Ru dispersions. First, the Ru precursor ($Ru(acac)_3$) was dissolved in acetone. Then the support was added to this solution. After being stirred at room temperature for 2 h, this slurry was heated to evaporate the acetone. It was then dried at 393 K overnight. The obtained powder was reduced in the gas flow of H_2 (50 SCCM) and Ar (50 SCCM) for 2 h.

Activity tests

Activity tests were conducted using a fixed bed flow-type reactor equipped with a quartz tube (8.0 mm o.d., 6.0 mm i.d.), as shown in Fig. S1 (ESI†). The catalyst (100 mg) was pre-reduced at 723 K for 2 h under a flow of $H_2 : Ar = 1 : 3$ (100 SCCM). When the electric field was imposed, two stainless steel electrodes were attached to the top and bottom of the catalyst bed. Then direct current was applied using a DC power supply. The response voltage was monitored using an oscilloscope (TDS 3052B; Tektronix Inc.). It was stable (0.2–0.4 kV), not forming discharge/plasma during the reaction. The overall actual catalyst bed temperature was measured using a thermocouple inserted into the bottom of the catalyst bed, the local catalyst surface temperature was measured using an NIR camera, and the atomic temperature was measured by evaluating the Debye–Waller (DW) factor (coherent neutron scattering caused by thermal motion) using EXAFS measurements,[16] and the effect of Joule heat caused by the electric field imposed was negligible in the promotion of the catalytic activity, selectivity to products, in this case. After removal of the produced H_2O using a cold-trap, the outlet gases including CO, CH_4, and CO_2 were

analyzed using a GC-FID (GC-14B; Shimadzu Corp.) equipped with a Porapak N packed column and a methanizer (Ru/Al_2O_3 catalyst). The respective calculation formulae for CO_2 conversion, CO selectivity and CO_2 consumption rate are shown below.

$$CO_2\ \text{conversion}\ (\%) = (F_{CO,out} + F_{CH_4,out})/F_{CO_2,in} \times 100 \quad (2)$$

$$CO\ \text{selectivity}\ (\%) = F_{CO,out}/(F_{CO,out} + F_{CH_4,out}) \times 100 \quad (3)$$

$$\text{Carbon balance}\ (\%) = \frac{\text{Carbon moles of output compounds (CO, } CH_4\text{, and } CO_2\text{)}}{\text{Carbon moles of input } CO_2} \quad (4)$$

In these equations, F_{out} represents the product formation rate and F_{in} denotes the supply rate of the reactant feed gas. Carbon balances were calculated as almost 100% for all reactions. Only CO and CH_4 were detected as carbon-containing products, indicating carbon deposition as negligible for all cases in this work.

The reactant feed gas consisted of CO_2, H_2, and Ar (CO_2 : H_2 : Ar = 1 : 1 : 2, total flow rate: 100 SCCM) in the catalytic activity tests for comparison among catalysts synthesized with different methods or various supports, testing at various temperatures, and the evaluation of reaction stability with or without the electric field. In activity tests for evaluation of the H_2/CO_2 ratio in the feed gas on the RWGS activity, the reactant feed gases at various H_2/CO_2 ratios were arranged to the total flow rate of 50 SCCM and were diluted by Ar (50 SCCM). In activity tests for the evaluation of the contact time (W/F), the total flow rates changed to 20–200 SCCM with the $CO_2 : H_2 : Ar$ ratio fixed at 1 : 1 : 2. The CO formation rate denoted as r is assumed according to the following equation using the partial pressures of CO_2 and H_2.

$$r = kP_{CO_2}^{\alpha}P_{H_2}^{\beta} \quad (5)$$

Characterization of catalysts

The actual Ru loading weight of the catalysts was quantified from inductively coupled plasma optical emission spectrometry (ICP-OES, 5100 ICP-OES; Agilent Technologies Inc.). Using about 50 mg of the catalyst, supported Ru was dissolved in sodium hypochlorite (Kanto Chemical Co. Inc.). The supports were then separated by filtration. The measurement was conducted using these solutions based on calibration curves recorded in Ru solutions ranging from approximately 0 to 5 ppm. Later, the residual supports were melted using lithium tetraborate (Kanto Chemical Co. Inc.) at 1273 K and dissolved in nitric acid. However, no Ru was detected in samples derived from residues.

The catalyst surface morphology and the Ru particle size of the prepared catalysts were evaluated using a field emission transmission electron microscope (FE-TEM) equipped with an energy dispersive X-ray (EDX) spectrometer (JEM-2100F; JEOL Ltd). Each sample was dispersed ultrasonically in ethanol. Then the suspension was dropped onto a Cu micro-grid (NP-C15; Okenshoji Co. Ltd). The Ru particle size was found by calculating the mean values of more than 100 particles treated as spherical objects.

In situ diffuse reflectance infrared Fourier transform spectroscopy (DRIFTS) measurements were conducted using an FT-IR spectrophotometer (FT/IR-6200; Jasco Corp.) equipped with an MCT-M detector and a ZnSe window. For the application of the electric field, the DRIFTS cell was made of Teflon with pinholes to insert electrodes, as shown in Fig. S2 (ESI†). The sieved $Ru/ZrTiO_4$ catalysts (about 120 mg) were used as a sample. Before measurements, the catalyst was reduced at 573 K in an H_2 flow for 2 h. It was then purged in Ar flow for 1 h. First, background spectra were measured under Ar (40 SCCM) flow at 373 K (without the electric field) and 423 K (with the electric field). Then, after supplying the reactant gas ($CO_2 : H_2 : Ar$ = 1 : 1 : 2, total flow rate: 40 SCCM), the measurement began at 373–673 K (without the electric field) and 423–573 K (with the electric field). When applying the electric field, 1 mA of direct current was imposed to minimize spectral distortion. All spectra from measurements were recorded with 4 cm^{-1} resolution and 100 scans.

To confirm the redox phenomena on the catalyst surface, H_2-TPR (temperature programmed reduction) was performed in a dilute hydrogen atmosphere with and without the electric field. In the experiments, the catalyst was loaded into a reaction tube, then it was pre-treated at 523 K in a hydrogen atmosphere for 1 h. At this temperature, only Ru was thermally reduced. Then, after purging the gas, the temperature was controlled from 523 K to 773 K at a ramping rate of 5 K min^{-1} while observing the hydrogen consumption (m/z = 2) and the formation of water (m/z = 18) using a Q-Mass (OmniStar/ThermoStar GSD350; Pfeiffer Vacuum Co. Ltd) with/without the electric field. Also, the transient response of the electric field application was observed at a constant temperature of 423 K immediately after the field was applied.

Results and discussion

After initial screening tests, we have chosen 1.5 wt% Ru-supported catalysts for this purpose (see Table S2, ESI†). Also, we prepared two 1.5 wt% Ru-supported catalysts: one is prepared by the Ru-colloid supporting method and the other is an impregnation method. The comparison between these two catalysts in the electric field is presented in Table 1. The CO selectivity over the impregnated catalyst was only 24.7%, but the colloidal nanoparticle deposited catalyst showed high RWGS selectivity (95.9%) with a similar CO_2 conversion in a kinetic region (11.2% for the colloidal Ru-catalyst and 9.7% for the impregnated Ru-catalyst, respectively). As a result of the TEM measurement (see Fig. S3, ESI†), the colloidal nanoparticle supported catalyst showed a fine dispersion of Ru, and the average Ru particle size was 2.37 nm; on the other hand, the

Table 1 Comparison of the RWGS activity over Ru catalysts with different Ru particle sizes in the electric field

Catalysts	Average Ru particle size/nm	Catalyst-bed temperature/K	Response voltage/V	CO_2 conversion/%	CO selectivity/%	CO formation rate per input power/mmol kJ^{-1}	TOF-s[b]/s^{-1}	TOF-p[c]/s^{-1}
1.5 wt% $Ru/ZrTiO_4$[a] (Ru colloids supported)	2.37	511	274	11.2	95.9	1.30	0.617	0.369
1.5 wt% $Ru/ZrTiO_4$ (impregnation method)	7.97	510	262	9.7	24.7	0.303	5.85	11.8

$CO_2:H_2:Ar$ = 1 : 1 : 2; 100 SCCM total flow rate; 100 mg catalyst weight; 5.0 mA imposed current. [a] The Ru loading weight was evaluated from the ICP-OES measurement. [b] TOF-s means the turnover frequency determined by the surface area of the metal particles. [c] TOF-p means the turnover frequency determined by the periphery of the metal particles.

impregnated catalyst showed a 7.97 nm particle size. The colloidal nanoparticle supported catalyst after the reaction with the electric field was also observed and the average Ru particle size was calculated to be 2.28 nm (Fig. S4, ESI†), which indicates that the Ru nanoparticles were not agglomerated in the reaction even with the application of the electric field. From these results, the highly dispersed Ru catalyst is appropriate for the selective RWGS reaction in the electric field. Therefore, for further investigation, we chose the colloidal nanoparticle supported $Ru/ZrTiO_4$ catalyst (hereafter denoted as the Ru(col)/$ZrTiO_4$ catalyst) as the best catalyst for RWGS in the electric field at a low temperature.

The electric field effects on the catalytic activity were investigated through activity tests conducted with and without the electric field at various temperatures (Fig. 1). Results indicated that the reaction proceeded even at a low temperature of 423 K, at which no activity was observed in the conventional RWGS reaction without the electric field, and that the selectivity was maintained higher than 90%. Furthermore, Arrhenius plots based on these tests (Fig. 2) showed that the apparent activation energy (6.74 kJ mol^{-1}) with the electric field was much lower than that without the electric field (64.5 kJ mol^{-1}), suggesting that the RWGS reaction with the electric field is promoted by a different mechanism from that of the conventional catalytic reaction without the electric field. The RWGS activity in the electric field was also evaluated by changing the imposed current. The results of the RWGS activity and the response voltage are shown in Fig. S5–S7, ESI.† In fact, the CO_2 conversion increased in proportion to the imposed current (power), whereas the CO selectivity remained almost constant at more than 90%, irrespective of the imposed current.

Next, the reaction stability was evaluated with and without the electric field. The results are summarized in Fig. 3. The activity without the electric field decreased gradually over time: 56.6% decrease of the initial activity in 24 hours. On the other hand, the activity when subjected to an electric field was almost stable for the next 50 hours, although it dropped a little at the beginning. After reaction for 120 min in the case of the test with/without the electric field, the catalyst was purged with each component of the feed gas (Ar, H_2, and CO_2), then the activity was evaluated. As depicted in Fig. S8 – left in the ESI,† the RWGS activity without the electric field decreased and recovered by the greatest degree when purged with H_2, which can be attributed to the removal of the CO_2-derived adsorbates. On the other hand, it was found that the catalyst could easily recover from the initial slight decrease in activity when purged with any of the gases (Fig. S8 – right in the ESI†). We believe that this initial slight decrease in activity is due to weak adsorption, and that this weak adsorption of intermediates is

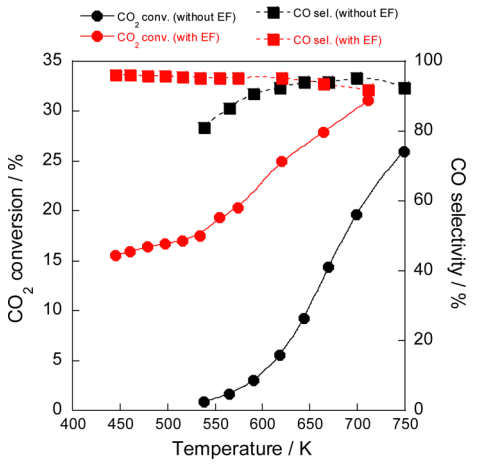

Fig. 1 Temperature dependence of CO_2 conversion and CO selectivity in the RWGS reaction with/without the electric field (EF) over the Ru(col)/$ZrTiO_4$ catalyst; $CO_2:H_2:Ar$ = 1 : 1 : 2; 100 SCCM total flow rate; 100 mg catalyst weight; 0 or 5.0 mA imposed current.

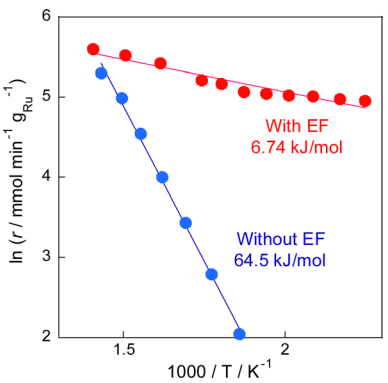

Fig. 2 Arrhenius plots for the RWGS reaction over the Ru(col)/$ZrTiO_4$ catalyst with and without the electric field; $CO_2:H_2:Ar$ = 1 : 1 : 2; 100 SCCM total flow rate; 100 mg catalyst weight; 0 or 5.0 mA imposed current.

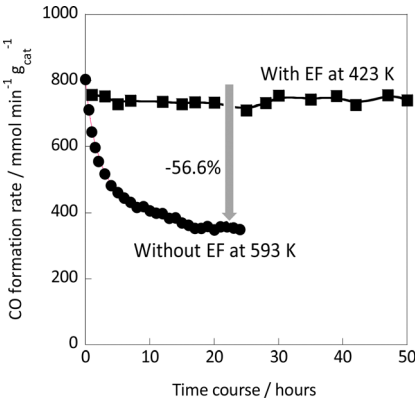

Fig. 3 Catalytic stability during the RWGS reaction over the Ru(col)/$ZrTiO_4$ catalyst with/without the electric field (5 mA); $CO_2 : H_2 : Ar$ = 1 : 1 : 2; total flow rate: 100 SCCM; 100 mg catalyst weight.

the reason why the catalyst can maintain stable and high catalytic performance thereafter.

Next, the effects of the H_2/CO_2 ratio of the reactant gas on CO and CH_4 formation rates were examined (Fig. 4). In the conventional RWGS reaction system, as the H_2 concentration of the feedstock gas increased, CH_4 formation proceeded dominantly and the CO_2 consumption rate (CO formation rate + CH_4 formation rate) decreased gradually with increasing CO_2 concentration. However, in the system with the electric field, high RWGS selectivity was achieved even in the H_2-rich condition. Moreover, the total CO_2 consumption rate increased concomitantly in the CO_2-rich condition, in contrast to the behavior observed without the electric field. These results revealed that the application of the electric field can suppress the side reaction (CO_2 methanation).

To clarify the influence of CH_4 formation, the influence of the contact time (W/F) on the catalytic activity was assessed (see Fig. S9, ESI†). In the thermal reaction system, the CO selectivity decreased considerably with increasing contact time. In the electric field, however, it is noteworthy that the CO selectivity remained higher than 90%, even in the high contact-time region. According to earlier reports,[30,31] the dependence between the contact time and CO (or CH_4) selectivity indicates

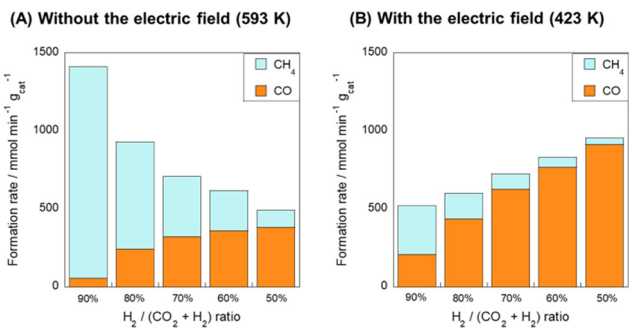

Fig. 4 CO and CH_4 formation rate over the Ru(col)/$ZrTiO_4$ catalyst under various H_2/CO_2 ratios (A) without the electric field at 593 K and (B) with the electric field (5 mA) at 423 K; 100 SCCM total flow rate; 100 mg catalyst weight.

that the reaction path of CO_2 methanation goes through CO intermediates, *i.e.*, the hydrogenation of CO on the Ru surface is the factor of the CH_4 byproduct in RWGS.

The results presented above imply that the imposed electric field contributed to suppression of CO hydrogenation on the Ru surface. We can propose that this enhancement of selectivity is attributable to the surface protonics induced by the electric field, which facilitates hydrogen migration from the Ru surface to the support. A part of dissociatively adsorbed hydrogen is generally known to be transferred to the support. However, residual dissociated H atoms on the active metal can react with CO to form CH_4. Considering another effect of the excess hydrogen on the Ru surface, it is claimed that electrons transfer from the hydrogen adsorbed onto Ru to the adsorbed CO *via* the metal. In this case, the Ru–C bond becomes stronger because of back-donation effects, making it more difficult to desorb.[32] A recent study has revealed that CO_2 hydrogenation using catalysts with high and low hydrogen-spillover ability dominates CO formation and CH_4 formation, respectively.[33] However, in the system with the electric field, as reported from experiments conducted with several systems of electric field promoted reactions, the induced surface proton conduction enables fast transfer of hydrogen on the catalyst surface.[14–16] In our recent study, surface proton conduction over metal oxides has been observed even under an H_2-dry atmosphere using electrochemical impedance spectroscopy.[34] Indeed, it was also found that when applying the electric field to ammonia synthesis using Ru catalysts, hydrogen poisoning on the active metal surface, which is regarded as the main cause of the degradation of the activity in conventional thermal reactions, is eliminated.[15] In general, hydrogen spillover accompanies electron transfer such as strong metal–support interaction (SMSI). Some room exists for the investigation of electric field effects, as discussed in the next section.

To elucidate the RWGS reaction mechanism in the electric field, *in situ* DRIFTS measurements were performed for comparison. First, DRIFTS spectra were measured without an electric field under the reaction atmosphere at 373–673 K. As shown in Fig. 5 and Fig. S10 in the ESI,† the IR feature developed after introduction of the reactant feed gas. Regarding carbonaceous species, CO adsorbed linearly (2012 cm^{-1}) or bridged (1885 cm^{-1}) on Ru was observed, whereas no band of gas-phase CO was detectable.[35–37] Furthermore, the bands at 1357 cm^{-1} and 1601 cm^{-1} represent different vibrational modes of formates,[38,39] which are most pronounced in the range of 1300–1700 cm^{-1} and which are found to be the main adsorbed species on the surface in this temperature region. The bands at 1669 cm^{-1} were assigned to bicarbonate species,[33,40,41] but their intensity decreased considerably as the temperature increased from 373 K to 473 K. When the temperature exceeded 573 K, the formate band intensity decreased gradually, which corresponded to the increasing intensity of gaseous CO bands, indicating that the formate species are the main intermediates in the reaction.

In earlier reports on the conventional RWGS reaction, mainly two mechanisms have been proposed: the associative mechanism and the redox mechanism.[42] In the associative

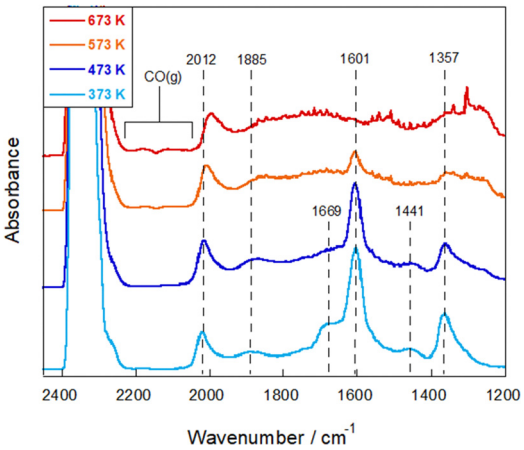

Fig. 5 *In situ* DRIFTS spectra under the RWGS reaction atmosphere over the Ru(col)/$ZrTiO_4$ catalyst without the electric field at 373–673 K; CO_2 : H_2 : Ar = 1 : 1 : 2; 40 SCCM total flow rate.

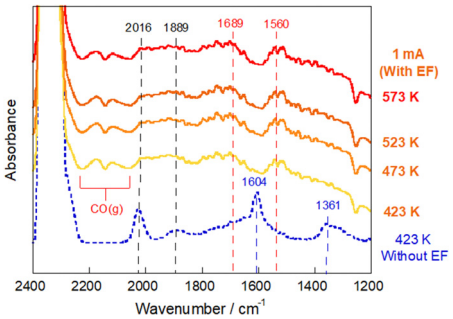

Fig. 6 *In situ* DRIFTS spectra under the RWGS reaction atmosphere over the Ru(col)/$ZrTiO_4$ catalyst recorded before/during application of the electric field (EF) at 423–573 K; CO_2 : H_2 : Ar = 1 : 1 : 2; 40 SCCM total flow rate.

mechanism, CO is produced *via* the decomposition of CO_2-derived intermediates such as formate and carbonate species, which are formed in the reaction with the hydrogen species on the supports.[43,44] In the redox mechanism, CO_2 is dissociated into CO using oxygen vacancies in metal oxides. These vacancies are regenerated by H_2 as a reducing agent.[45,46] On a support with less reducibility, which makes it difficult for oxygen vacancies to be generated, formate species are known to form preferentially; the associative path becomes predominant.[42] Moreover, formate species can stably present on the surface, which often accumulates on the surface and sometimes causes poisoning of the catalyst.[47,48] Accordingly, one can infer that degradation of the activity over time without the electric field, as described above, can be attributed to the strong adsorption of formate species over the catalyst surface or CO species on the Ru surface. In earlier work, the activation energy barrier involving the formation and decomposition of formate species has been estimated to be about 50–70 kJ mol^{-1},[42,49,50] which is close to our experimental value calculated with the Arrhenius plot.

In situ DRIFTS measurements were conducted by applying the electric field at various temperatures (Fig. 6). We were able to observe a marked change in adsorbed species after imposing the electric field: the formate peak intensity decreased drastically, whereas the gas CO band developed and some carbonaceous bands newly appeared. The bands at 1560 cm^{-1} and 1689 cm^{-1} were assigned, respectively, to bidentate carbonate[51,52] and carboxylate species.[53,54] Additionally, the DRIFTS spectrum when the imposed current was increased up to 10 mA, was measured (Fig. S11, ESI†) and the increase of gaseous CO species was observed corresponding to the evolution of the carboxylate and bidentate carbonate species. Considering the enhancement of the RWGS activity with the value of the imposed current (Fig. S5–S7, ESI†), this result suggests that carboxylate and carbonate species can be responsible for the CO formation in the electric field. These species were reported to form preferentially in the presence of oxygen vacancies and, especially, the carboxylate species was reported to be more reactive than formate species.[22,42,55] In earlier studies of electrically assisted catalytic reactions, the electric field can activate surface lattice oxygens in metal oxides, which play an important role in the reaction with reactants at low temperatures.[56] The findings obtained from this study also provide insight into the possibility that an electric field can promote the generation of oxygen vacancies and contribute to CO_2 activation.

To ensure the reaction mechanism in the electric field, the ESR measurements were conducted using samples before and after applying the electric field (Fig. S12, ESI†). In both samples, sharp signals at g = 2.002 attributed to the surface-embedded Ti^{3+} sites[57–60] were detected. In general, the formation of V_o (oxygen vacancy) requires the reduction of metal cations adjacent to the lattice oxygen (*e.g.* $Ti^{4+} \rightarrow Ti^{3+}$), so these sites are combined with the oxygen vacancy in the bulk. In addition, a broad signal assigned to surface-exposed Ti^{3+} sites was also observed only on catalyst treated in H_2 flow with the electric field.[56–61] According to a previous report,[59] the presence of surface oxygen vacancies, which can play a role in the surface catalytic reaction, can be accompanied by the manifestation of this peak. Therefore, this result suggests that the electric field can efficiently introduce oxygen vacancies preferentially at the surface rather than the bulk under the reaction conditions through promoting the reduction of surface metal cations.

To confirm these phenomena, H_2-TPR was performed in a dilute hydrogen atmosphere with and without the electric field. In the experiments, the catalyst was pre-reduced at 523 K in a hydrogen atmosphere, so only Ru was thermally reduced. Results are shown in Fig. S13 in the ESI;† for the TPR without the electric field, hydrogen was consumed and reacted with lattice oxygen to form water only above 623 K. On the other hand, as shown in Fig. S14 in the ESI,† for the TPR with the electric field, the results show that hydrogen is consumed and reacts with the lattice oxygen of the catalyst support to form water and lattice vacancies after the application of the electric field, even at a low temperature of 423 K. The surface oxygen consumption and vacancy formation corresponded to about five layers of surface oxygen in $ZrTiO_4$. Thus, it was experimentally confirmed that the lattice oxygen reacts and forms lattice defects even at low temperatures in the electric field.

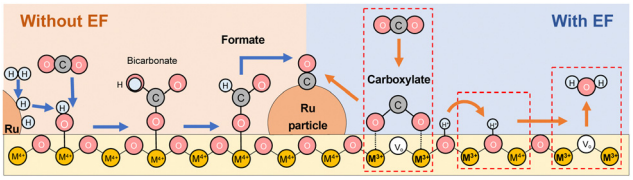

Fig. 7 The schematic illustration of the proposed mechanism in the RWGS reaction with or without the electric field over the Ru(col)/$ZrTiO_4$ catalyst.

Discussion

Based on these results, we considered the reaction mechanism with and without an electric field in RWGS. Fig. 7 presents the proposed RWGS mechanism with/without the electric field over the Ru/$ZrTiO_4$ catalyst. In the conventional thermal RWGS reaction (Fig. 7: left), CO_2 initially reacts with the hydroxyl species on the $ZrTiO_4$ surface, resulting in the formation of bicarbonate, which transforms into formate. This reaction path, however, proceeds quickly, considering the limited presence of bicarbonate species at low temperatures in DRIFTS spectra. Finally, these formate species decompose to CO at temperatures higher than 573 K. Generally, formate species at the metal–support interface can be involved in the series of reactions, whereas other species far from the support lack reactivity.[49] On the other hand, in the system with the electric field (Fig. 7: right), CO_2 adsorbs on the support in the form of carboxylate species using an oxygen vacancy. The vacancy could be formed mainly at the metal–support interface due to the modification of the electronic band structure (the Schottky junction).[62] Subsequently, this intermediate dissociates into CO, followed by the release of water through the protonation of the surface lattice oxygen, leading to oxygen vacancy regeneration.

Specifically for the electron acceptance and donation in the redox system of this reaction, the proposed reaction pathway is found to comprise the following elementary reaction steps:

$$H_2 \rightarrow 2H^+ + 2e^- \quad (6)$$

$$2H^+ + M^{4+} - O_{lat}{}^{2-} - M^{4+} + 2e^- \rightarrow H_2O + M^{3+} - V_O^{\bullet\bullet} - M^{3+} \quad (7)$$

$$CO_2 + M^{3+} - V_O^{\bullet\bullet} - M^{3+} \rightarrow CO + M^{4+} - O_{lat}{}^{2-} - M^{4+} \quad (8)$$

Initially, the hydrogen dissociatively adsorbed onto the Ru surface migrates to the $ZrTiO_4$ support as H^+ (oxidative part: eqn (6)). These H^+ species react with the surface lattice oxygens to form vacancies (V_o), accompanied by the reduction of adjacent metal cations (M; Zr or Ti) in the support (reductive part: eqn (7)). Finally, CO_2 is converted into CO entering into oxygen vacancies (eqn (8)). It was reported that defect sites could be introduced into the catalyst under the condition in which surface hydrogen migration occurred. Yamazaki *et al.* explained the mechanism of the formation of the oxygen vacancy assisted by hydrogen spillover based on the electron transfer between the band gaps. When the dissociated H atoms spill over onto the metal oxide to form hydroxyl species, electrons derived from H atoms are donated to the conduction band and some of these electrons are transferred to the mid-gap states. Subsequently, the oxygen vacancy can be formed when the electrons further trap into the defect level below the mid-gap states.[59] As described above, the oxidation part (surface protonics) improves CO selectivity; the reduction part is associated with the CO_2 activation. Therefore, both reaction parts are connected with factors that are important for the promotion of the RWGS activity.

Many methods of applying an electric field to the reaction tube itself or to the catalyst layer have been reported recently,[63–65] but these are promoted by heating by Joule heat, and the reaction mechanism is the same as that of an ordinary heated catalyst. On the other hand, in the case shown in this paper where a DC electric field is applied to a catalyst with a semiconductor as a support and a fine metal, the reaction mechanism is different from that of a catalyst heated as described above. Although Joule heat is generated to some extent by the application of the electric field, its contribution to the reaction activity, selectivity, and mechanism is very small. As for the effect of temperature, the overall catalyst layer temperature was measured using a thermocouple, the local catalyst surface temperature was measured using a NIR camera, and the atomic temperature was measured by evaluating the DW factor (coherent neutron scattering caused by thermal motion) using EXAFS measurements.

Therefore, we conclude that the electric field accelerates this charge transfer (6 & 7), which contributes to the achievement of high activity at low temperatures.

Conclusions

This study revealed that highly dispersed Ru catalysts exhibit high RWGS activity with the application of an electric field in the low-temperature region, where no activity was observed in the conventional heated catalytic RWGS reaction. In contrast to catalysts with larger Ru particles, the highly dispersed Ru catalysts showed high CO selectivity. Moreover, in the electric field, the catalyst maintained high CO selectivity under high H_2 concentration or short contact time. This finding can be explained by surface protonics: fast hydrogen migration to the support restrains the side reaction of CO with residual hydrogen species on the Ru surface. Regarding the reaction mechanism, the RWGS reaction without the electric field proceeds through the formate-mediated path, followed by decomposition to CO. In the case of the reaction with the electric field, the main reaction path shifts to the redox mechanism, through which the generated oxygen vacancies can participate in CO_2 activation at low temperatures. Consequently, the electric field promotes both the surface hydrogen migration and redox reaction using lattice oxygen vacancies, resulting in high RWGS activity and selectivity even at low temperatures and in a stoichiometric condition.

Conflicts of interest

The authors have no conflict of interest.

Acknowledgements

The authors thank Shinpei Enomoto (Kagami Memorial Research Institute for Materials Science and Technology, Waseda University) for great assistance in the FE-TEM operations and EDS measurements. The ESR measurement was conducted using the research equipment (Material Characterization Central Laboratory) shared in the MEXT Project for promoting public utilization of advanced research infrastructure (Program for supporting construction of core facilities) under Grant Number JPMXS0440500022. The TPR measurement (Fig. S13/S14) was conducted by Ms Ayaka Shigemoto, Waseda Univ. Some catalyst preparation and other experiments were assisted by Mr. Gao Yusuan, Waseda Univ.

References

1 International Energy Agency, Net Zero by 2050-A Roadmap for the Global Energy Sector, see **https://www.iea.org/reports/net-zero-by-2050**, accessed on 30 Oct/2022.
2 P. Gabrielli, M. Gazzani and M. Mazzotti, *Ind. Eng. Chem. Res.*, 2020, **59**(15), 7033–7045.
3 W. Wang, S. Wang, X. Maa and J. Gong, *Chem. Soc. Rev.*, 2011, **40**, 3703–3727.
4 P. Frontera, A. Macario, M. Ferraro and P. Antonucci, *Catalyst*, 2017, **7**(2), 59.
5 Y. A. Dazza and J. N. Kuhn, *RSC Adv.*, 2016, **6**, 49675–49691.
6 M. Behrens, F. Studt, I. Kasatkin, S. Kühl, M. Hävecker and F. Abild-Pedersen, *Science*, 2012, **336**(6038), 893–897.
7 S. Ba, Q. Shao, P. Wang, Q. Dai, X. Wang and X. Huang, *J. Am. Chem. Soc.*, 2017, **139**(20), 6827–6830.
8 K. Zhao, X. Nie, H. Wang, S. Chen and X. Quan, *Nat. Commun.*, 2020, **11**, 2455.
9 R.-P. Ye, J. Ding, W. Gong, M. D. Argyle, Q. Zhong, Y. Wang, C. K. Russell, Z. Xu, A. G. Russell, Q. Li, M. Fan and Y.-G. Yao, *Nat. Commun.*, 2019, **10**, 5698.
10 D. Gao, R. M. Arán-Ais, H. S. Jeon and B. R. Cuenya, *Nat. Catal.*, 2019, **2**, 198–210.
11 J. Ran, M. Jaroniec and S.-Z. Qiao, *Adv. Mater.*, 2018, **30**, 1704649.
12 J.-I. Makiura, T. Higo, Y. Kurosawa, K. Murakami, S. Ogo, H. Tsuneki, Y. Hashimoto, Y. Sato and Y. Sekine, *Chem. Sci.*, 2021, **12**, 2108–2113.
13 R. Snoeckx and A. Bogaerts, *Chem. Soc. Rev.*, 2017, **46**, 5805–5863.
14 R. Manabe, S. Okada, R. Inagaki, K. Oshima, S. Ogo and Y. Sekine, *Sci. Rep.*, 2016, **6**, 38007.
15 R. Manabe, H. Nakatsubo, A. Gondo, K. Murakami, S. Ogo, H. Tsuneki, M. Ikeda, A. Ishikawa, H. Nakai and Y. Sekine, *Chem. Sci.*, 2017, **8**, 5434–5439.
16 Y. Hisai, Q. Ma, T. Qureishy, T. Watanabe, T. Higo, T. Norby and Y. Sekine, *Chem. Commun.*, 2021, **57**, 5737–5749.
17 K. Oshima, T. Shinagawa, Y. Nogami, R. Manabe, S. Ogo and Y. Sekine, *Catal. Today*, 2014, **232**, 27–32.
18 T. Yabe, K. Mitarai, K. Oshima, S. Ogo and Y. Sekine, *Fuel Process. Technol.*, 2017, **158**, 96–103.
19 T. Yabe, K. Yamada, K. Murakami, K. Toko, K. Ito, T. Higo, S. Ogo and Y. Sekine, *ACS Sustainable Chem. Eng.*, 2019, **7**(6), 5690–5697.
20 T. Yabe, K. Mitarai, K. Oshima, S. Ogo and Y. Sekine, *J. CO2 Util.*, 2017, **20**, 156–162.
21 K. Yamada, S. Ogo, R. Yamano, T. Higo and Y. Sekine, *Chem. Lett.*, 2020, **49**, 303–306.
22 S. Kattel, P. Liu and J. G. Chen, *J. Am. Chem. Soc.*, 2017, **139**(29), 9739–9754.
23 Y. Wang, L. R. Winter, J. G. Chen and B. Yan, *Green Chem.*, 2021, **23**, 249–267.
24 J. C. Matsubu, V. N. Yang and P. Christopher, *J. Am. Chem. Soc.*, 2015, **137**(8), 3076–3084.
25 J. H. Kwak, L. Kovarik and J. Szanyi, *ACS Catal.*, 2013, **3**(11), 2449–2455.
26 A. Aitbekova, L. Wu, C. J. Wrasman, A. Boubnov, A. S. Hoffman, E. D. Goodman, S. R. Bare and M. Cargnello, *J. Am. Chem. Soc.*, 2018, **140**(42), 13736–13745.
27 K. Kusada, H. Kobayashi, T. Yamamoto, S. Matsumura, N. Sumi, K. Sato, K. Nagaoka, Y. Kubota and H. Kitagawa, *J. Am. Chem. Soc.*, 2013, **135**, 5493–5496.
28 C. Bock, C. Paquet, M. Couillard, G. A. Botton and B. R. MacDougall, *J. Am. Chem. Soc.*, 2004, **126**, 8028–8037.
29 Y. Chen, K. Y. Liew and J. Li, *Mater. Lett.*, 2008, **62**, 1018–1021.
30 X. Chen, X. Su, H. Duan, B. Liang, Y. Huang and T. Zhang, *Catal. Today*, 2017, **281**, 312–318.
31 D. J. Pettigrew and D. L. Trimm, *Catal. Lett.*, 1994, **28**, 313–319.
32 A. Erdöhelyi, M. Pásztor and F. Solymosi, *J. Catal.*, 1986, **98**, 166–177.
33 X. Li, J. Lin, L. Li, Y. Huang, X. Pan, S. E. Collins, Y. Ren, Y. Su, L. Kang, X. Liu, Y. Zhou, H. Wang, A. Wang, B. Qiao, X. Wang and T. Zhang, *Angew. Chem., Int. Ed.*, 2020, **59**, 19983–19989.
34 Y. Hisai, K. Murakami, Y. Kamite, Q. Ma, E. Vøllestad, R. Manabe, T. Matsuda, S. Ogo, T. Norby and Y. Sekine, *Chem. Commun.*, 2020, **56**, 2699–2702.
35 S. Ø. Stub, E. Vøllestad and T. Norby, *J. Phys. Chem. C*, 2017, **121**(23), 12817–12825.
36 A. Takahashi, R. Inagaki, M. Torimoto, Y. Hisai, T. Matsuda, Q. Ma, J. G. Seo, T. Higo, H. Tsuneki, S. Ogo, T. Norby and Y. Sekine, *RSC Adv.*, 2020, **10**, 14487.
37 S. Y. Chin, C. T. Williams and M. D. Amiridis, *J. Phys. Chem. B*, 2006, **110**(2), 871–882.
38 Y. Wang, S. Kattel, W. Gao, K. Li, P. Liu, J. G. Chen and H. Wang, *Nat. Commun.*, 2019, **10**, 1166.
39 N. H. M. D. Dostagir, R. Rattanawan, M. Gao, J. Ota, J. Hasegawa, K. Asakura, A. Fukouka and A. Shrotri, *ACS Catal.*, 2021, **11**, 9450–9461.
40 X. Wang, Y. Hong, H. Shi and J. Szanyi, *J. Catal.*, 2016, **343**, 185–195.
41 X. Wang, H. Shi, J. H. Kwak and J. Szanyi, *ACS Catal.*, 2015, **5**, 6337–6349.
42 L. F. Bobadilla, J. L. Santos, S. Ivanova, J. A. Odriozola and A. Urakawa, *ACS Catal.*, 2018, **8**(8), 7455–7467.

43 S. Choi, B.-I. Sang, J. Hong, K. J. Yoon, J.-W. Son, J.-H. Lee, B.-K. Kim and H. Kim, *Sci. Rep.*, 2017, **7**, 41207.
44 D. Heyl, U. Rodemerck and U. Bentrup, *ACS Catal.*, 2016, **6**(9), 6275–6284.
45 J. Wang, C.-Y. Liu, T. P. Senftle, J. Zhu, G. Zhang, X. Guo and C. Song, *ACS Catal.*, 2020, **10**(5), 3264–3273.
46 S. Mine, T. Yamaguchi, K. W. Ting, Z. Maeno, S. M. A. H. Siddiki, K. Oshima, S. Satokawa, K.-I. Shimizu and T. Toyao, *Catal. Sci. Technol.*, 2021, **11**, 4172–4180.
47 A. Goguet, F. C. Meunier, D. Tibiletti, J. P. Breen and R. Burch, *J. Phys. Chem. B*, 2004, **108**(52), 20240–20246.
48 E. T. Saw, U. Oemar, M. L. Ang, H. Kus and S. Kawi, *Catal. Sci. Technol.*, 2016, **6**, 5336–5349.
49 F. C. Meunier, D. Reid, A. Goguet, S. Shekhtman, C. Hardacre, R. Burch, W. Deng and M. Flytzani-Stephanopoulos, *J. Catal.*, 2007, **247**, 277–287.
50 X. Wang, H. Shi and J. Szanyi, *Nat. Commun.*, 2017, **8**, 513.
51 X. Jia, X. Zhang, N. Rui, X. Hu and C. Liu, *Appl. Catal., B*, 2019, **244**, 159–169.
52 S. T. Korhonen, M. Calatayud and A. O. I. Krause, *J. Phys. Chem. C*, 2008, **112**, 16096–16102.
53 L. Liu, C. Zhao and Y. Li, *J. Phys. Chem. C*, 2012, **116**, 7904–7912.
54 H. He, P. Zapol and L. A. Curtiss, *J. Phys. Chem. C*, 2010, **114**(49), 21474–21481.
55 J. A. Rodríguez, J. Evans, J. Graciani, J.-B. Park, P. Liu, J. Hrbek and J. F. Sanz, *J. Phys. Chem. C*, 2009, **113**, 7364–7370.
56 N. Nakano, M. Torimoto, H. Sampei, R. Yamashita, R. Yamano, K. Saegusa, A. Motomura, K. Nagakawa, H. Tsuneki, S. Ogo and Y. Sekine, *RSC Adv.*, 2022, **12**, 9036–9043.
57 S. Mohajernia, P. Andryskova, G. Zoppellaro, S. Hejazi, S. Kment, R. Zboril, J. Schmidt and P. Schmuk, *J. Mater. Chem. A*, 2020, **8**, 1432–1442.
58 F. Amano, M. Nakata, A. Yamamoto and T. Tanaka, *J. Phys. Chem. C*, 2016, **120**, 6467–6474.
59 Y. Yamazaki, K. Mori, Y. Kuwahara, H. Kobayashi and H. Yamashita, *ACS Appl. Mater. Interfaces*, 2021, **13**, 48669–48678.
60 Y. Yamazaki, T. Toyonaga, N. Doshita, K. Mori, Y. Kuwahara, S. Yamazaki and H. Yamashita, *ACS Appl. Mater. Interfaces*, 2022, **14**, 2291–2300.
61 E.-M. Köck, M. Kogler, T. Bielz, B. Klötzer and S. Penner, *J. Phys. Chem. C*, 2013, **117**, 17666–17673.
62 J. C. Frost, *Nature*, 1988, **334**, 577–580.
63 S. T. Wismann, J. S. Engbæk, S. B. Vendelbo, F. B. Bendixen, W. L. Eriksen, K. Aasberg-Petersen, C. Frandsen, I. Chorkendorff and P. M. Mortensen, *Science*, 2019, **364**(6442), 756–759.
64 Q. Dong, Y. Yao, S. Cheng, K. Alexopoulos, J. Gao, S. Srinivas, Y. Wang, Y. Pei, C. Zheng, A. H. Brozena, H. Zhao, X. Wang, H. E. Toraman, B. Yang, I. G. Kevrekidis, Y. Ju, D. G. Vlachos, D. Liu and L. Hu, *Nature*, 2022, **605**, 470–476.
65 X. Mei, X. Zhu, Y. Zhang, Z. Zhang, Z. Zhong, Y. Xin and J. Zhang, *Nat. Catal.*, 2021, **4**, 1002–1011.